

Design of a Small, Axial-Flux Permanent-Magnet Motor

M. Van Dessel, R. Belmans, R. Hanitsch, E. A. Hemeed

Abstract

The paper deals with the design of a disc-type motor excited by permanent magnets. The main flux is oriented in the axial direction, yielding a pan-cake type arrangement. The outer diameter is about 45 mm, the axial length about 15 mm. After the introduction, the motor design is explained. On the basis of these general design considerations, the average flux density at no-load in the materials is approximated using an analytical, one-dimensional approach. An accurate analysis of the axial flux machine requires a 3D finite-element calculation. The 3D model design needed for this, is explained. The motor characteristics (induced voltage and torque), obtained from the 3D calculation are described and compared with measurements.

1 Introduction

In computer peripherals, office equipment and storage devices, the trend is towards small packages, low power consumption, high efficiency and low cost. Consequently, the drives required by this type of equipment, need to have a small rotor inertia and a small volume. In a number of applications the disc-type motor is the best choice because of its short axial length. Also for portable devices where the energy is supplied by a battery, there is crucial demand for a drive system with a high efficiency. To attain these goals, permanent magnets are used for the excitation and an electronic commutation can be combined with speed control.

As permanent-magnet material, Nd-Fe-B has recently become very attractive. It shows the highest energy density of all commercially available materials. It provides high air-gap flux density and makes a highly dynamic motor design feasible. To be able to make the best possible use of the material, the design has to be optimised using numerical field analysis techniques.

2 Motor Design

2.1 Design Features

The main design features of the motor are:

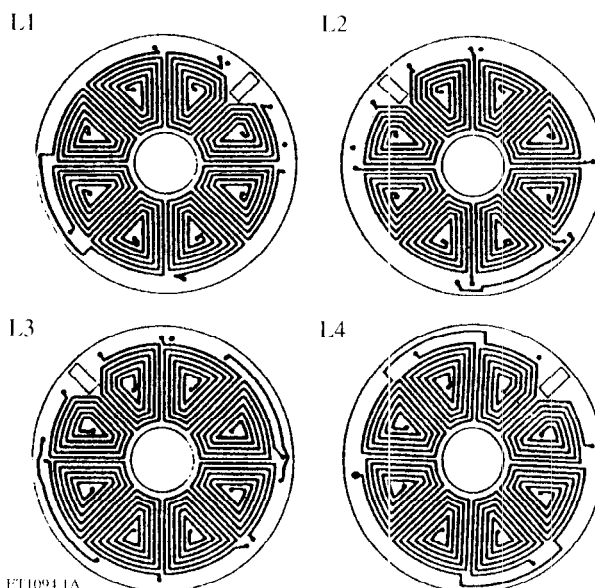
- the armature winding is on the stator;
- the rotor consists of a thin disc made of sintered permanent-magnet material in a multipole arrangement;
- for the detection of the rotor position, magneto-resistive sensors are used.

Brushless axial field motors can be built using a symmetrical or asymmetrical layout [1, 2]. The prototype design is characterised by symmetrical planar windings, produced using etching techniques. The required torque makes it necessary to employ a multilayer winding to establish a sufficiently high current layer.

2.2 Description of the Design

The prototype features two phases on the stator and eight poles on the rotor. The rotor is a disc-type permanent magnet, magnetised in the axial direction.

The stator consists of two disks of ferromagnetic back-iron material with two air-gap windings. On each stator side, eight windings are installed and connected forming two phases. Each winding consists of four layers. In the second stator disk, the opposite connections are made to balance the electrical system. Geometrically, both stator parts are identical. However, they are rotated with respect to each other. This unsymmetrical winding arrangement reduces the axial forces on the machine bearings. **Fig. 1** shows the printed circuit boards of the four layers in detail. **Fig. 2** shows the winding arrangement. From **Fig. 3** the main dimensions of the prototype can be taken. The outer diameter is about 45 mm, axial length about 15 mm.



ET11094.1A

Fig. 1. Printed circuit boards of the four layers L1 to L4 of the winding

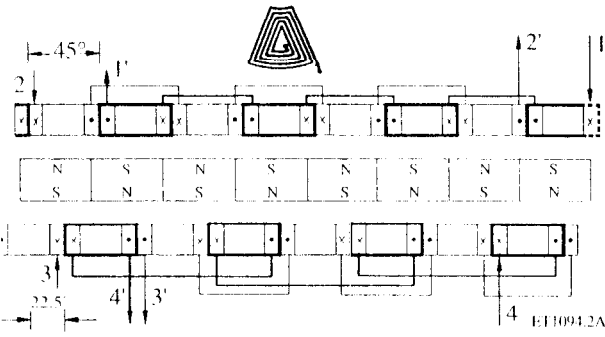


Fig. 2. Winding arrangement

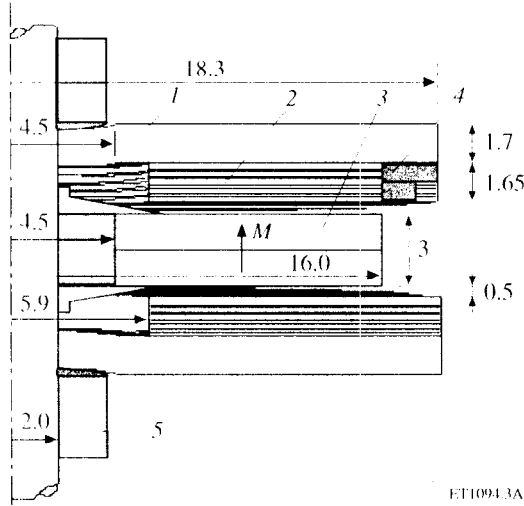


Fig. 3. Main dimensions (in mm) of the prototype (1 magnetic back iron; 2 etched winding; 3 rotating magnetic disc; 4 position sensor; 5 bearing)

3 Analytical No-Load Average Flux-Density Distribution

The geometry is shown in Fig. 4, including the overall flux pattern. Since the magnetic periodicity of the rotor is 90°, the motor model consists of a sector of 90°. The magnetic south pole is located under the first winding of the upper stator. The magnetic north pole is located under the second winding. The aim of the analytical calculation is to obtain average values of flux density B in the materials using a simplified magnetic circuit. The approximation is done in a cylindrical surface cutting through the centre points of the winding turns (these are indicated by groups M1 and M2). The cylindrical cross-section is given in Fig. 5.

The flux in the air is generated by the magnets and is divided into the main flux and the leakage flux:

$$B_{Air} S_{Air} = \Phi_M - \Phi_\sigma = \Phi_M (1 - \sigma) = B_M S_M (1 - \sigma). \quad (1)$$

The quantities in eq. (1) are determined as follows. S_M is the area of one north or one south pole, each occupying an angle of 45° (R_2 is the outer radius of the magnet and R_1 the inner radius):

$$S_M = \frac{\pi(R_2^2 - R_1^2)}{8}. \quad (2)$$

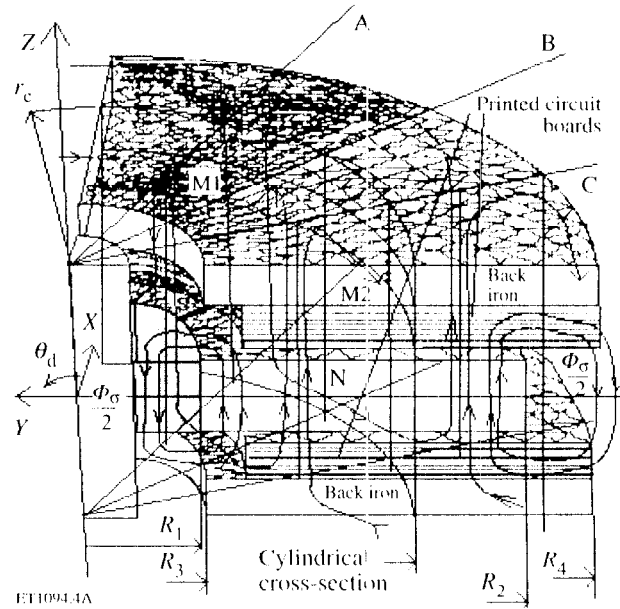


Fig. 4. Geometry of the disc-type rotor and overall flux pattern

S_{Air} is the area of the air, perpendicular to the flux path and also taken over 45°. The area to be considered follows from the configuration of the windings that magnetically behave as air and are glued to the back iron. From the front of Fig. 4, it can be seen that the surface S_{Air} has to be taken equal to the iron area $S_{Fe,v}$ over an angle of 45°. $S_{Fe,v}$ is the surface of the iron, perpendicular to the useful flux entering and leaving the iron vertically. The air at the inside of the windings and the windings themselves are taken together in the area S_{Air} . R_4 is the outer radius of the windings and R_3 the inner radius of the iron:

$$S_{Air} = S_{Fe,v} \frac{\pi(R_4^2 - R_3^2)}{8}. \quad (3)$$

Φ_σ is the leakage flux, i. e. the flux not reaching the iron. This flux passes through the air, but has no net effect through the area S_{Air} . The leakage flux avoids the iron at the outer radius of the magnet disc and at the non-magnetic shaft. The leakage flux establishes closed loops passing through the magnets. An estimation of the leakage factor σ is 0.05 to 0.20.

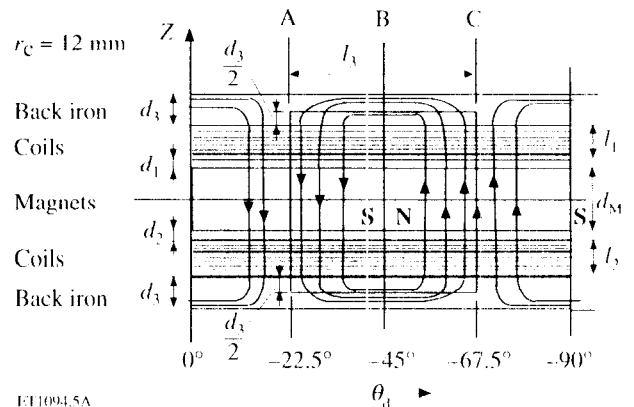


Fig. 5. Development of the cylindrical cross-section

The useful flux in the air and the printed circuit board, coming from the magnetic north pole, enters the iron vertically accounting for the conservation of the magnetic flux at the interface:

$$S_{\text{Air}} B_{\text{Air}} = S_{\text{Fe},v} B_{\text{Fe},v} \quad (4)$$

$B_{\text{Fe},v}$ is the flux density in the iron in the vertical direction. Once in the iron, the flux turns in horizontal direction and splits into two partial fluxes:

$$\Phi_{\text{Fe},h} = \frac{B_{\text{Fe},v} S_{\text{Fe},v}}{2} = \hat{B}_{\text{Fe},h} S_{\text{Fe},h} \quad (5)$$

$S_{\text{Fe},h}$ is the vertical cross-section of the iron, perpendicular to the partial flux (in front of Fig. 4):

$$S_{\text{Fe},h} = d_3(R_4 - R_3) \quad (6)$$

$\hat{B}_{\text{Fe},h}$ is the maximum value and $\bar{B}_{\text{Fe},h}$ is the average value of horizontal flux density. $B_{\text{Fe},h}(\theta_0)$ follows a triangular pattern in the back iron, assuming a linear behaviour of the material:

$$\hat{B}_{\text{Fe},h} = 2\bar{B}_{\text{Fe},h} \leq 1.0 \text{ T} \quad (7.a)$$

$$\bar{H}_{\text{Fe},h} = \frac{\hat{H}_{\text{Fe},h}}{2} \quad (7.b)$$

In Fig. 5 the closed flux path is given. Ampere's law at zero current yields:

$$\begin{aligned} H_M d_M + H_{\text{Air}}(d_1 + l_1) + H_{\text{Fe},v} \frac{d_3}{2} + \bar{H}_{\text{Fe},h} l_3 + H_{\text{Fe},v} \frac{d_3}{2} \\ + H_{\text{Air}}(d_1 + l_1) + H_M d_M + H_{\text{Air}}(d_2 + l_2) + H_{\text{Fe},v} \frac{d_3}{2} \\ + \bar{H}_{\text{Fe},h} l_3 + H_{\text{Fe},v} \frac{d_3}{2} + H_{\text{Air}}(d_2 + l_2) = 0. \end{aligned} \quad (8)$$

Due to the symmetry of upper and lower disks $d_1 = d_2$ and $l_1 = l_2$ such that H_{Air} and H_{Fe} are valid in the upper and lower portions. Also H_M is present twice due to symmetry. $\bar{H}_{\text{Fe},h}$ is the average horizontal field strength and l_3 is the length of the flux path in the iron:

$$\int_{l_3} H_{\text{Fe},h} dl = \bar{H}_{\text{Fe},h} l_3 \quad \text{with} \quad l_3 = \frac{\pi}{4} r_c \quad (9)$$

The magnetic characteristic of the air and the windings is a straight line (permeability of the free space):

$$B_{\text{Air}} = \mu_0 H_{\text{Air}} \quad (10)$$

The flux density value B_M is taken from the magnetisation characteristic of the magnet material used (Fig. 6).

From the material data of the slightly non-linear curve a least mean squares approximation is obtained. With the fitted B_{if} and μ_{rev} the following holds:

$$B_M = B_{\text{if}} + \mu_{\text{rev}} \mu_0 H_M \quad (11)$$

The magnetic characteristic for the back iron is given by $H_{\text{Fe},v} = f(B_{\text{Fe},v})$. For the maximum value of the horizontal flux density it is linearized and related to the vertical flux density using eq. (5):

$$\hat{H}_{\text{Fe},h} = f(\hat{B}_{\text{Fe},h}) = f\left(\frac{B_{\text{Fe},v} S_{\text{Fe},v}}{2 S_{\text{Fe},h}}\right) = \frac{S_{\text{Fe},v}}{2 S_{\text{Fe},h}} f(B_{\text{Fe},v}) \quad (12)$$

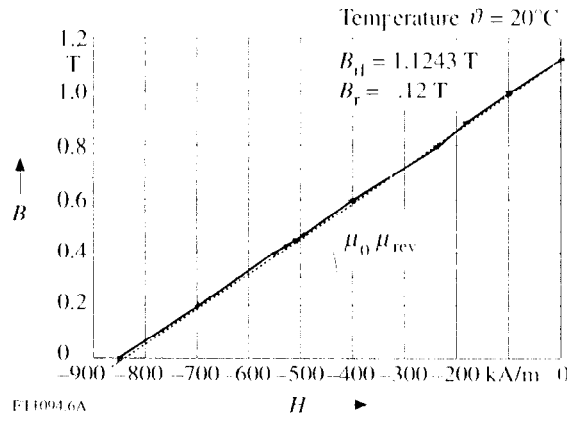


Fig. 6. Magnetisation curve of the permanent magnets with least mean squares fitted curve

From eqs. (1), (4), (5), (7a), (7b), (8), (10), (11) and (12) the system can be deduced:

$$B_A = \frac{B_{\text{Fe},v} S_{\text{Fe},v}}{S_A} \quad (13.a)$$

$$B_M = \frac{B_{\text{Fe},v} S_{\text{Fe},v}}{S_M(1-\sigma)} \quad (13.b)$$

$$H_{\text{Fe},v} = f(B_{\text{Fe},v}) \quad (13.c)$$

$$H_{\text{Fe},v} = \frac{\left(B_{\text{if}} - \frac{B_{\text{Fe},v} S_{\text{Fe},v}}{S_M(1-\sigma)} \right) \mu_0 \mu_{\text{rev}} - \frac{S_{\text{Fe},v} B_{\text{Fe},v}}{S_{\text{Air}} \mu_0} (d_1 + l_1 + l_2 + d_3)}{l_3 \frac{S_{\text{Fe},v}}{2 S_{\text{Fe},h}} + d_3} \quad (13.d)$$

From eqs. (13c) and (13d) follows that in order to obtain $B_{\text{Fe},v}$ one has to find the intersection between the iron curve with a straight line. The intersection is determined graphically (Fig. 7). The leakage $\sigma = 0.05$ as a first estimation, yielding $B_{\text{Fe},v} = 0.386 \text{ T}$.

If the parameter σ is varied for which only an estimate can be given anyway, the slope of the straight line is changed. By finding the intersection with the iron curve, different values are found (Tab. 1). It can be seen that when $\sigma \geq 0.10$, $\hat{B}_{\text{Fe},v} \leq 1.0 \text{ T}$ as required by the con-

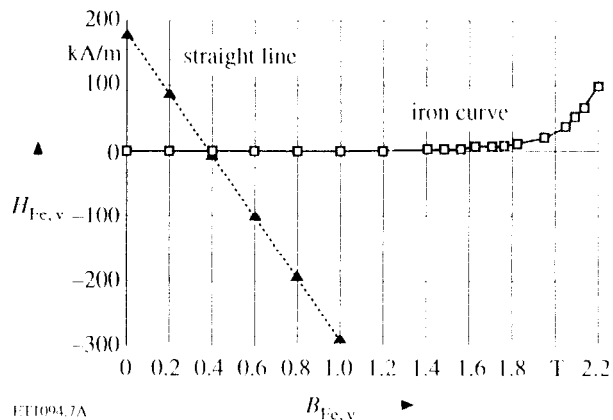


Fig. 7. Determination of $B_{\text{Fe},v}$ at the intersection of the iron curve with a straight line ($\sigma = 0.05$)

σ	$B_{Fe,v}$ (in T)	$\hat{B}_{Fe,h}$ (in T)	$\bar{B}_{Fe,h}$ (in T)	B_{Air} (in T)	B_M (in T)
0.00	0.395	1.041	0.520	0.395	0.527
0.05	0.386	1.016	0.508	0.386	0.542
0.10	0.376	0.989	0.495	0.376	0.557
0.15	0.365	0.961	0.481	0.365	0.573
0.20	0.354	0.931	0.466	0.354	0.590
0.25	0.342	0.900	0.450	0.342	0.608

Tab. 1. Variation of leakage factor σ

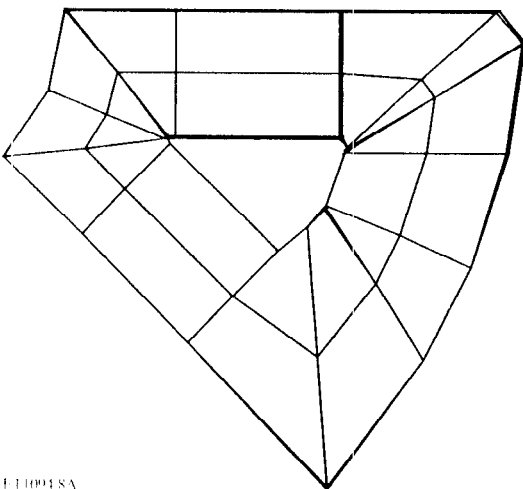
dition (7a). $\sigma > 0.20$ are not as the leakage flux would be too high. The best choice for $\sigma = 0.15$. The accompanying values for the flux densities are: $B_M = 0.573$ T, $B_{Fe,v} = 0.365$ T, $\hat{B}_{Fe,h} = 0.961$ T, $B_{Fe,h} = 0.481$ T. The average value for B_M is compared with the average calculated from the 3D finite-element analysis further on.

4 Finite-Element Analysis

4.1 General Overview

Because of its special geometry, this type of motor can not be analysed using a two-dimensional approach, as generally found in modern design procedures. Therefore, a three dimensional analysis is used. In the finite-element system used for the analysis, the vector-potential approach, generally applied in two-dimensional systems [3] is replaced with a magnetic scalar potential in the non-current carrying zones in combination with the influence of the currents, that are treated independently [4]. The coils are modelled separately and are brought into the mesh containing the magnetic system.

The first finite-element simulation is performed with the windings not carrying current. In the second finite-element solution, the flux-density distribution is obtained accounting for the combined action of permanent magnets and current carrying coils. This situation is difficult to handle using the finite-element model: the current in the coils is spread over all elements intersecting with the coil. Therefore, a sufficiently fine mesh has to be defined to correctly treat the windings.



F11094.8A

Fig. 8. Coil mesh for layer L1 of one winding

4.2 Coil Modelling

Due to the complicated shape and the limits set by the finite-element package on the number of elements, the coil models are simplified with respect to reality. Fig. 8 shows the mesh of layer L1 of a winding.

As can be seen, a hand winding representation is used, rather than modelling the full turns. For the field calculation this is sufficient:

- the same mmf is generated as in the real winding;
- the current transferred from the coil mesh to the elements of the material mesh is equivalent to the real model; the stator mesh does not match the coil outline, as will be explained further on.

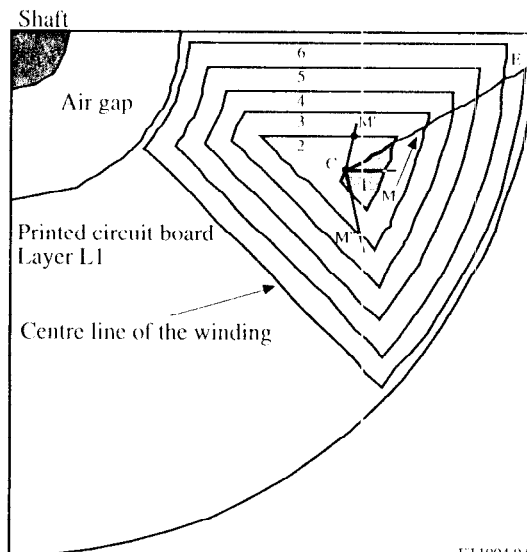
Therefore, by using this type of coil, the field is locally incorrect but globally, to integrate the flux and to calculate the torque, the approach is sufficiently accurate.

From Fig. 1 it can be seen that the differences among the eight windings are sufficiently small to represent them using the same shape. The numerical analysis is performed by using one four layer winding in the top stator and one in the bottom stator.

4.3 Stator Modelling

The motor model consists of a sector of 90° , since the periodicity of both stator and rotor is 90° . In Fig. 9 the mesh outline of the top layer L1 of one winding is shown. The outline of the winding corresponds to the centre line of the real winding.

Although the coils are modelled separately, the material mesh represented here needs the coil outline for the flux calculation. The flux calculation is performed by integrating the vertical component of the flux-density distribution B_z over the surface described by a line connecting a reference point C with a point M moving along the centre line of the winding. The reference point C is located at the centre of the winding. The integration process is illustrated in Fig. 9. The line from the reference point C to the outer end of the centre line E indicates



F11094.9A

Fig. 9. Outline of the mesh at the top layer L1 of a winding

where one turn of the centre line ends and the next one starts. It is noted that the area between two turns of the centre line is described several times by the line CM as it rotates around the centre. With Ψ_m being the flux in the area between centre line turns m and $(m - 1)$, the flux linkage for the 1st layer L1 becomes:

$$\Psi_{1,1} = (\Psi'_1) + (\Psi_1 + \Psi_2) + (\Psi_1 + \Psi_2 + \Psi_3) + \dots + (\Psi_1 + \dots + \Psi_6) = 6\Psi_1 + 5\Psi_2 + 4\Psi_3 + 3\Psi_4 + 2\Psi_5 + \Psi_6. \quad (14)$$

The integration has to be repeated for the other three layers of the winding. The calculated flux values in each layer add up giving the total flux linked with one winding, Ψ_w :

$$\Psi_w = \Psi'_{1,1} + \Psi'_{1,2} + \Psi'_{1,3} + \Psi'_{1,4}. \quad (15)$$

The stator mesh includes the centre line of the coil, but not the outline and therefore does not match a coil mesh if the latter follows the real coil outline. This is due to the limits set on the overall complexity of the material mesh, as explained further on.

4.4 Rotor Mesh

In Fig. 10 the layout of the rotor mesh is shown. The magnetic disc is divided into 20 segments of 4.5°, each having a different material label. When defining a magnetic problem using this model, all segments are given a material characteristic representing Nd-Fe-B. Ten segments are defined as a north pole, and ten as a south pole. By changing the north and south orientation of the labels when defining the next problem, a simulation of the stepwise rotation of the rotor is obtained. The calculation of the motor characteristics as a function of the rotor position is done without having to produce an other material mesh.

4.5 Base Plane

Although described as separate entities, in the actual model the rotor and stator originate from one base plane. This base plane contains the outline of both stator and rotor, and from it the finite element model is built by

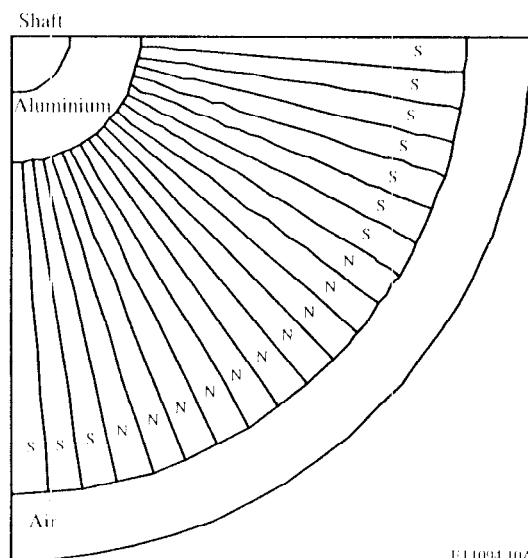


Fig. 10. Layout of the rotor mesh

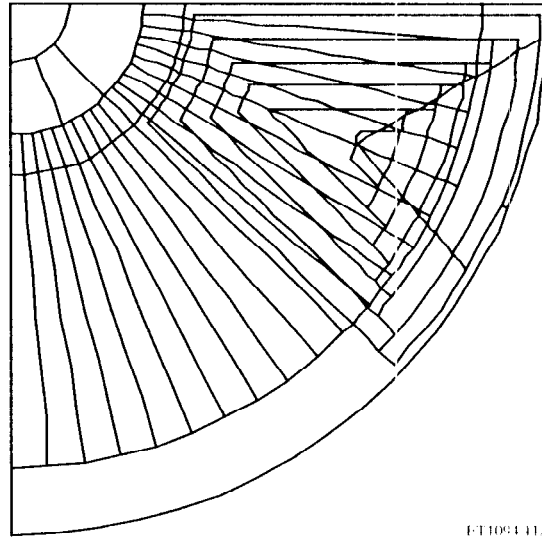


Fig. 11. Layout of the base plane of the mesh

extrusion [5]. This base plane has to be regarded as the superposition of all layouts of horizontal planes in the material mesh (Fig. 11).

After describing the stator and rotor meshes, it becomes clear why the base plane is so complicated. When starting to build the model, the base plane is the first outline to be drawn. All the separate regions require a material label. All the horizontal planes in the 3D mesh are copies from this base plane. In each of these copies a relabelling operation of all separate regions has to be done to get the required layout of each plane. Since seven different plane layouts are present, it is a very time consuming process. To keep this manageable, and because the number of separate regions in the base plane is limited, the coil layout in the stator has been limited to the centre line only. Together with the limit on the number of elements in the coil mesh, this explains why the band winding is chosen for the coil meshes.

5 Characteristics from the Finite-Element Analysis

5.1 Flux Couplings

The flux Ψ_w produced by the magnets and coupled with one winding, that does not carry any current, is calculated by integrating the flux density as described above (eqs.(14) and (15)). By a stepwise rotor motion, Ψ_w as a discrete function of the rotor position θ is obtained.

5.2 Induced Voltage in one Phase

Using the discrete Fourier transform, the linked flux Ψ_w can be expressed as a continuous function of θ and differentiated with respect to θ . This derivative is used to calculate the induced voltage in one phase formed by four windings in series:

$$U_{in-p} = -4 \frac{d\Psi_w}{d\theta} \frac{n 2\pi}{60}, \quad (16)$$

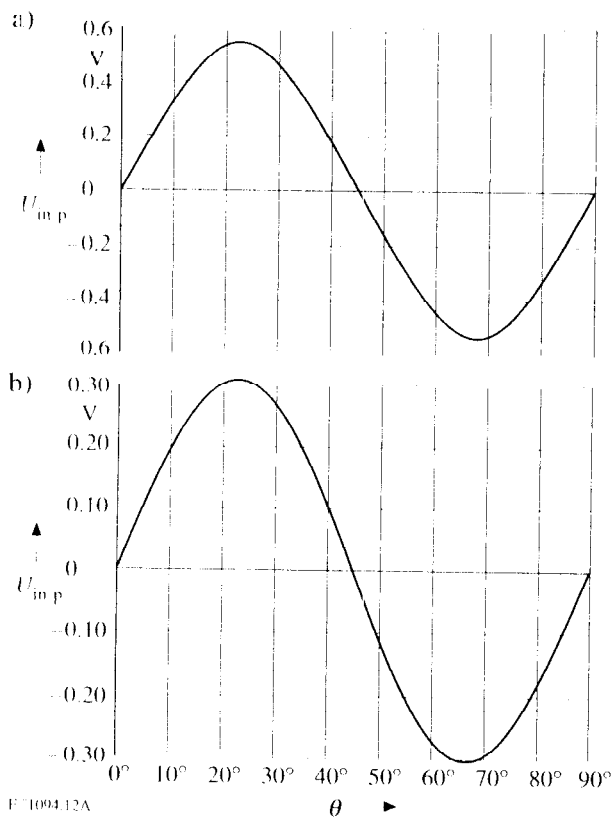


Fig. 12. Voltage U_{imp} induced in one phase at a rotor speed of 1000 rpm
 a) Calculated
 b) Measured

where n is the constant rotating speed in rpm. The induced voltage as a function of the angle θ at a speed of 1000 rpm is shown in **Fig. 12a**. This is an important macroscopic characteristic, since it can be compared with measured values. The result is a sine with an amplitude of 0.5447 V.

The measured curve is given in **Fig. 12b**. The amplitude is 0.31 V at 1000 rpm. The voltage is measured over two of the four layers of the windings so that the amplitude of the voltage over one phase is 0.62 V. The amplitude calculated from the finite-element simulation is 0.5447 V and thus 11 % lower than the measured one.

5.3 Inductance Calculation

The inductance of one phase (four windings) is:

$$L = \left(\frac{4}{i} \right) (\Psi_{w,i} - \Psi_{w,0A}) = 14 \mu\text{H}. \quad (17)$$

The current i in the phase is typically 0.5 A. is the flux linked with the winding due to the current and the permanent magnets, is the flux linkage produced by the magnets alone. The measured value is 11.8 mH and thus lower. Several elements contribute to this discrepancy.

- In the real motor, the back iron is laminated; however, it is very difficult in the model to represent the laminations correctly. This makes the magnetic reluctance smaller in the model, so that flux and inductance become larger.

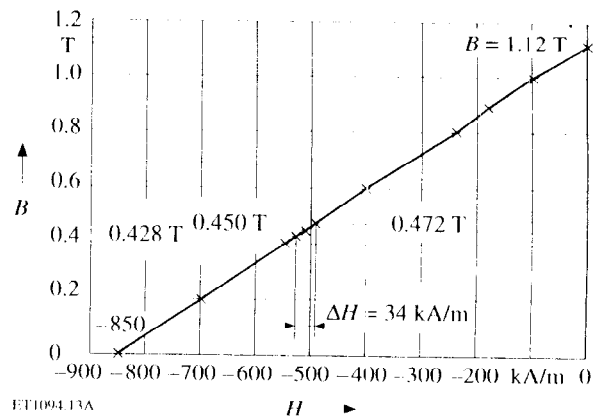


Fig. 13. Variation of the operating point on the magnetic characteristic

- In the model $\Psi_{\text{phase}} = 4\Psi_w$. In the real motor $\Psi_{\text{phase}} < 4\Psi_w$, because one of the four windings is smaller to provide space for the position sensor (Fig. 1).
- The coil is represented by a band winding and does not match the material mesh outline.

5.4 Flux Density on the Magnet Surface at Load Conditions

Fig. 13 represents the operating points on the magnetic characteristic:

- At zero current, the minimum B value at the magnet surface is 0.45 T, under the centre of the winding shown before. B is minimum there, if a north or a south pole is under the winding. The average B value on the upper magnet surface is then 0.69 T. The average calculated using the analytical model in paragraph 2 is about 0.53 T, being 23 % lower than the average from the numerical calculation.
- At rated operating conditions a current of 0.5 A flows in one phase of the top stator and one phase of the bottom stator.
- At short-circuit conditions, 5 A passes through both windings. When the north pole is under the top stator winding, the minimum value of B rises to 0.472 T. When the south pole is under the top stator winding, the minimum B value drops to 0.428 T. The magnetic field variation of 34 kA/m is more than 20 times smaller than the value of the coercivity. The variation of the operating points is thus acceptable.

5.5 Torque Calculation

5.5.1 Calculation Methods

Three methods have been investigated.

I. Interaction between current and flux density

The force per unit volume on current-carrying conductors is given by:

$$F_v = \mathbf{J} \times \mathbf{B}. \quad (18)$$

The force on a conductor is given by

$$\mathbf{F} = \int_0^l \mathbf{I} d\mathbf{l} \times \mathbf{B}. \quad (19)$$

The torque on the stator is obtained by integrating the torque contribution of the forces on the individual conductors:

$$\mathbf{T} = \int_0^l \mathbf{r} \times (\mathbf{I} d\mathbf{l} \times \mathbf{B}). \quad (20)$$

Only the z component of the stator torque is calculated. The rotor torque is the opposite of the torque acting on the stator.

II. Virtual work

The torque is given by derivative of the co-energy with respect to the rotor position:

$$T = \left. \frac{dW_{co}}{d\theta} \right|_{i=\text{const}}. \quad (21)$$

III. Maxwell Stress

Integrating the “Maxwell Stress Tensor” on a surface surrounding the rotor also yields the torque.

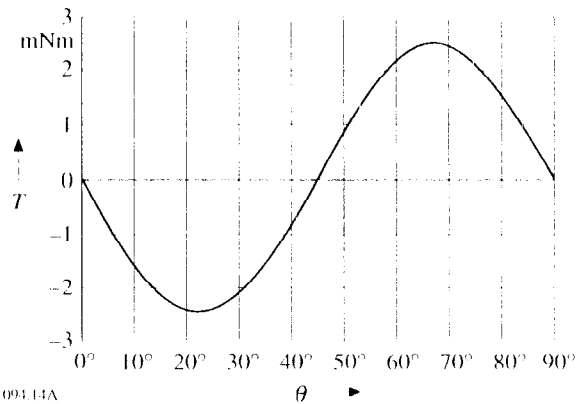
5.5.2 Conditions for the Torque Calculation

- The calculation is done under steady-state conditions: the developed torque is balanced by the load torque. The field is calculated under time-invariant conditions. Therefore, eddy currents are neglected, and a magnetostatic analysis is used.
- Under normal operating conditions two coils carry current: one in the top stator, one in the bottom stator. Due to linearity, this can be treated as the superposition of two cases with one active coil. Linearity is found by checking the operating points in the B - H characteristic of both the magnets and the back iron. Therefore, only the torque of one of the four coils is calculated by the finite-element analysis. The torque produced by the other three coils can be obtained from the one that is calculated using an appropriate time shift.
- The finite-element calculation is done on a quarter of the motor geometry. As four corresponding windings in each quarter are connected in series to form one of the coils, the torque developed by the coil is four times larger.
- The calculation is done over an angle of 90° (one pole pitch), where 20 positions are considered, spaced at 4.5° . The current in the winding is constant and equals 0.5 A.

5.5.3 Results

I. Interaction between current and flux density

The motor torque developed on the rotor when one coil is active, is represented in **Fig. 14** as a function of



ET1094.14A

Fig. 14. Torque obtained from current - field interaction (First winding supplied with 0.5 A)

the rotor position. Applying a “Discrete Fourier Transform” (DFT) on the calculation results, the curve can be described by:

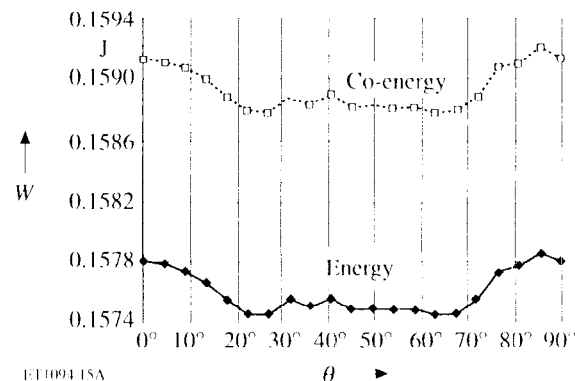
$$T = -2.466 \sin(4\theta) \quad (\text{in mNm}). \quad (22)$$

II. Virtual work

Fig. 15 shows the energy and co-energy stored in a $1/4$ motor versus the rotor position. Given the dips and bumps in the curves, the calculated quantities are not sufficiently accurate to perform a straightforward differentiation. The values of the co-energy show only significant variations in the third and fourth digit. Digits 5 to 7 are meaningless since the co-energy value given by the 3D solver is the result of a very large amount of numerical operations. If a 20 point DFT is performed to calculate the average value and ten harmonic components, the result obtained is firmly influenced by these conditions. The harmonic coefficients are calculated to construct the derivative curve (**Fig. 16**). It is obviously meaningless to serve as the torque curve.

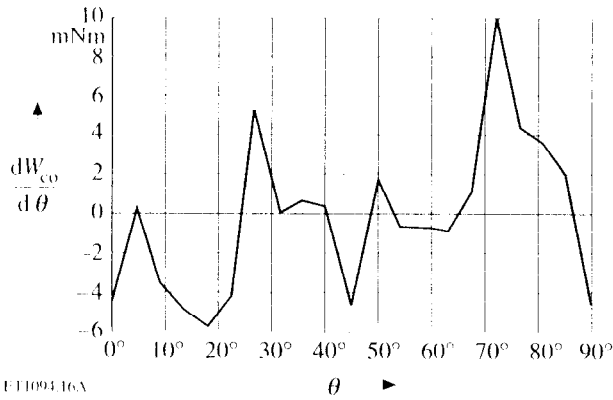
To be able to get meaningful results from the co-energy values, the theoretical curve is considered. Since the theoretical torque is given by a sine function as in **Fig. 14**, the co-energy should be a single-frequency cosine:

$$W_{co} = \bar{W}_{co} + A_1 \cos(4\theta). \quad (23)$$



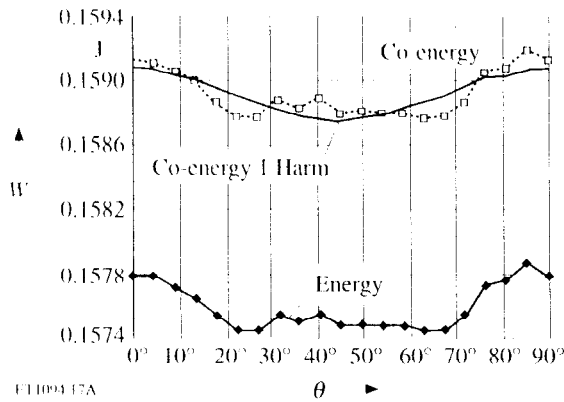
ET1094.15A

Fig. 15. Energy and co-energy in $1/4$ of the motor (first winding supplied with 0.5 A)



E11094.16A

Fig. 16. Derivative of co-energy for full motor



E11094.17A

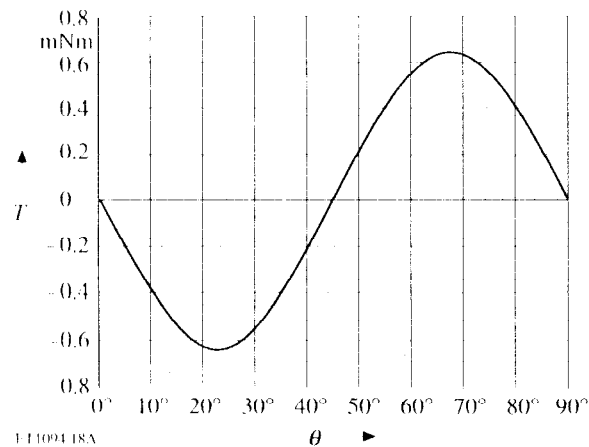
Fig. 17. First harmonic fitted to the co-energy curve (Fig. 15) (first winding supplied with 0.5 A)

In Fig. 15 it is possible to fit a cosine to the co-energy curve by calculating the average $\overline{W_{co}}$ and the first harmonic A_1 , using the 20 data-points for the DFT (Fig. 17).

The corresponding derivative gives the torque from the fitting procedure:

$$\frac{dW_{co}}{d\theta} = -4A_1 \sin(4\theta). \quad (24)$$

This is given in Fig. 18 with an amplitude equal to $4A_1 = 0.636$ mNm. For the full motor with four windings in series, the torque amplitude is $4(4A_1) = 2.544$ mNm.



E11094.18A

Fig. 18. Torque obtained from first harmonic fit of co-energy (first winding supplied with 0.5 A)

This value matches well the result obtained in the current-field interaction method being 2.466 mNm.

III. Maxwell Stress

The Stress tensor has to be evaluated on a surface enclosing the rotor. In the 3D finite-element package, only flat surfaces can be used to constitute a closed volume. In case of the model of the quarter disc-type motor, the planes can be put between the rotor and the stators (one above the rotor, one underneath). The cylindrical circumference of the rotor cannot be closed by a flat plane, because the model ends at the circumference of the stator leaving not enough place for a flat plane outside the rotor.

T_{mz} is the contribution of the upper plane to the component of the rotor torque around the z-axis and is given by:

$$T_{mz} = v_0 \iint_u B_z(xB_y - yB_x) dS, \quad (25)$$

while the contribution of the lower plane to that torque T_{rlz} is:

$$T_{rlz} = -v_0 \iint_l B_z(xB_y - yB_x) dS. \quad (26)$$

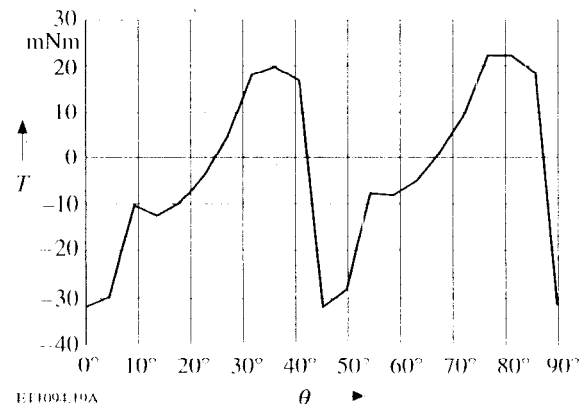
The minus sign arises because the tensor has to be evaluated with dS being associated with an outward pointing normal vector. For the lower plane, this points opposite to the z-axis.

The resulting torque is:

$$T_{\tau z} = T_{mz} + T_{rlz}. \quad (27)$$

The torque curve as calculated from the Maxwell stress tensor on both planes is given in Fig. 19. Clearly, it disagrees with the torque as calculated in Fig. 14 and Fig. 18. The reasons for this are the following:

- Although the field is small at the circumference of the rotor, it can have a significant contribution to the Maxwell stress integration. According to the tensor theory, its components have the dimensions of stress but only the integral value has a physical meaning. Maybe leaving out the circumference surface introduced an error larger than anticipated.
- Since the calculation gives a zero order B field, the accuracy is limited.
- The mesh is not optimised for Maxwell stress integration.



E11094.19A

Fig. 19. Torque obtained from Maxwell stresses (first winding supplied with 0.5 A)

– Since B_x and B_y are small compared to B_z , they are not accurate enough to serve as multiplicands. When investigating colour plots from the solution, one can see that in the plane where the Maxwell formulae are evaluated B_x and B_y are only significant around the radial lines lying above the separation lines between north and south poles in the magnet rotor. At those places, B_z is low and passes through zero. The result is that the integrand is not accurately calculated. On a colour plot of the integrand one can see that positive and negative areas nearly cancel each other. Before multiplying by v_0 , the result of the integration is a number in the order of 10^{-9} . The sign and magnitude vary almost randomly with the rotor position (Fig. 19).

5.5.4 Resulting Torque Curve when four Coils are Operating

Fig. 20 shows the four torque curves resulting from operating the four coils over one period. The basic curve is the torque T_1 obtained from the current-field interaction method (Fig. 14). The other three are calculated from T_1 by shifting the curves in time:

$$\begin{aligned} T_2(\theta) &= T_1(\theta + 45^\circ), \\ T_3(\theta) &= T_1(\theta + 22.5^\circ), \\ T_4(\theta) &= T_1(\theta + 67.5^\circ). \end{aligned} \quad (28)$$

Fig. 20 also gives the resulting torque (dotted curve) when switching is done for a counter-clock-wise rotation. This means that only the coils giving a positive torque are active. In this four-coil configuration it means that at every position, two coils are active: one in the top, one in the bottom stator. The properties of the sum torque are:

- a periodicity of 22.5° (1/4 of motor periodicity);
- an average $\bar{T} = 3.14$ mNm;
- a peak to peak ripple of 1.02 mNm.

The theoretical average power produced by the motor, including power lost by friction, is:

$$\bar{P} = \bar{T} \frac{n 2\pi}{60}. \quad (29)$$

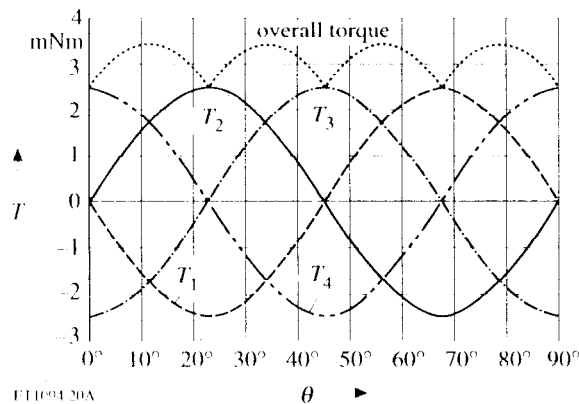


FIGURE 20A
Fig. 20. Torque curves for the disc-type motor (windings supplied with 0.5 A)

If the rotation speed n equals 1000 rpm, the power $\bar{P} = 0.329$ W.

5.5.5 Comparison with Measured Torques

For the permanent-magnet motor the amplitude of torque and induced voltage are given by:

$$\hat{T} = C_T i. \quad (30)$$

$$\hat{U} = C_U \omega. \quad (31)$$

C_U is measured from the induced voltage curve in Fig. 12b:

$$C_U = \frac{\hat{U}}{\omega} = \frac{0.62 \text{ V}}{\left(\frac{2\pi \cdot 1000}{60 \text{ s}} \right)} = 5.92 \cdot 10^{-3} \text{ Vs}. \quad (32)$$

With $C_T = C_U$ and $i = 0.5$ A, the estimated value of the torque amplitude is:

$$\hat{T}_{\text{est}} = C_T i = 2.96 \text{ mNm}. \quad (33)$$

This is comparable to the calculated amplitude in eq. (22): 2.466 mNm.

6 Conclusions

In this paper a small, axial flux permanent magnet motor is analysed. The geometry makes a 3D analysis necessary for accurate results. Since analytical methods are restricted to one or two dimensions, use has to be made of a finite-element package for the 3D analysis. This requires the design of a model not only representing the geometry, but also allowing the implementation of procedures to calculate motor characteristics. Because the 3D model has to be extruded out of one base plane, one has to limit the number of details in the structure.

The calculated motor characteristics are:

- induced voltage in one phase,
- inductance of one phase,
- operating-point variation of the magnets,
- electromagnetic torque developed when four phases are operated.

The macroscopic parameters are comparable to the ones obtained by measurements on a prototype. Future work includes the analysis of an even smaller disc-type motor based on the experience achieved in the analysis of this particular machine.

7 List of symbols

Ψ_m	flux linked with zone m in one layer
$\Psi_{l,k}$	flux linked with layer k of one winding
Ψ_w	flux linked with one winding
Ψ_{phase}	flux linked with one phase
θ	angular position of the rotor
$U_{\text{in p}}$	induced voltage in the coil (one phase)
W_{co}	co-energy
T_k	torque when coil k is switched on

References

- [1] *Park, C.-S.*: Theoretische und experimentelle Untersuchungen an einem elektronisch kommutierten Scheibenläufer-Kleinstmotor. Diss. TU Berlin/Germany, 1989
- [2] *Hanitsch, R.; Park, C.-S.*: Performance of a sub fractional HP disc-type motor. Int. Conf. on Electr. Mach. (ICEM'90), MIT, Cambridge/USA 1990, Conf.-rec. vol. 1, pp. 138 - 142
- [3] *Lowther, D. A.; Silvester, P. P.*: Computer-Aided Design in Magnetics. Berlin/Germany: Springer, 1985
- [4] *Webb, J. P.; Forghani, B.*: A single scalar potential method for 3D magnetostatics using edge elements. IEEE Trans. on Magn. TM-25 (1989) no. 5, pp. 4 126-4 128
- [5] MagNet User Manual for Release 4.01. Montreal/Canada: Infolytica Corp., 1991

Acknowledgements

The authors are grateful to the Commission of the European Communities for funding the research work within the BRTE-EuRAM framework, project no. BE-3360. The authors are indebted to the Belgian Nationaal Fonds voor Wetenschappelijk Onderzoek for its financial support for this work and the Belgian Ministry of Scientific Research for granting the project IUAP No. 51 on Magnetic Fields.

Manuscript received on March 14, 1994

The Authors



Michel Van Dessel (1967) received the M.S. degree in Electrical Engineering from the Katholieke Universiteit Leuven, Belgium, in 1990. From 1990 until the present, he has been a member of the staff of the Electrical Machines and Drives Laboratory of the Katholieke Universiteit (K.U.), Leuven, Dept. of Electrical Engineering. He obtained a Ph.D. degree from the K.U. Leuven in 1995. He is currently working as a lecturer at the Mechelen Polytechnic (De Naeyer). (Katholieke Universiteit Leuven, Dept. of Electrical Engineering, Electrical Energy, Kardinaal Mercierlaan 94, B-3001 Heverlee-Leuven, Belgium, T +32 16/2209 31-1020, Fax + 32 16/29 3064)



Ronnie Jozef Maria Belmans (1956) received the M.S. degree in electrical engineering from the Katholieke Universiteit, Leuven, Belgium in 1979, the Ph.D. degree from the same university in 1984 and the Special Doctorate in 1989. He got the "Habilitation" from the RWTH in Aachen, Germany. From 1979 to 1985, he was a member of the staff of the Katholieke Universiteit

Leuven. Currently, he is at the same place Professor, teaching electrical machines and drives. His research interests include electrical machine design (permanent magnet and induction motors), computer-aided engineering, and vibrations and audible noise in electrical machines. From October 1988 till September 1989 he worked at the Laboratory for Electrical Machines of the RWTH Aachen, Germany, as a "Von Humboldt Fellow". From October 1989 till September 1990, he was a Visiting Associate Professor at McMaster University, Hamilton, Canada. He has been visiting lecturer at Imperial College in London, UK, in 1991. Since October 1993 he is "Privatdozent" of the RWTH in Aachen. He is a member of the Editorial Board of ETEP. (Katholieke Universiteit Leuven, Dept. of Electrical Engineering, Electrical Energy, Kardinaal Mercierlaan 94, B-3001 Heverlee-Leuven, Belgium, T +32 16/2209 31-1020, Fax +32 16/32 1985)



Rolf Hanitsch (1940), VDE, is Professor of Electrical Engineering (electrical machines and drives) at the Technical University (TU) Berlin, Germany, Institute of Electrical Machines (since 1976). Research activities are on special electric motors, micro-motors, reliability, advanced control of drives, power electronics and photovoltaics. (TU Berlin, Institut für Elektrische Maschinen, Einsteinufer 11, D-10587 Berlin/Germany, T +49 30/3 14-22403, Fax +49 30/3 14-2 11 33)



Elsayed A. Hemeed (1943) received the M.S.E.E. degree from the Technical University (TU) Berlin, Germany, in 1986. He is researcher at the Institute of Electrical Machines, TU Berlin. His research interests are modelling, control and design of electrical machines, micro-motors and power electronic applications. (TU Berlin, Institut für Elektrische Maschinen, Einsteinufer 11, D-10587 Berlin/Germany, T +49 30/3 14-25704, Fax +49 30/3 14-2 11 33)